



Cite this: *Phys. Chem. Chem. Phys.*,
2014, 16, 22321

A novel approach for analyzing electrochemical properties of mixed conducting solid oxide fuel cell anode materials by impedance spectroscopy

A. Nenning,* A. K. Opitz, T. M. Huber and J. Fleig

For application of acceptor-doped mixed conducting oxides as solid oxide fuel cell (SOFC) anodes, high electrochemical surface activity as well as acceptable electronic and ionic conductivity are crucial. In a reducing atmosphere, particularly the electronic conductivity of acceptor-doped oxides can become rather low and the resulting complex interplay of electrochemical reactions and charge transport processes makes a mechanistic interpretation of impedance measurements very complicated. In order to determine all relevant resistive and capacitive contributions of mixed conducting electrodes in a reducing atmosphere, a novel electrode design and impedance-based analysis technique is therefore introduced. Two interdigitating metallic current collectors are placed in a microelectrode, which allows in-plane measurements within the electrode as well as electrochemical measurements *versus* a counter electrode. Equivalent circuit models for quantifying the spectra of both measurement modes are developed and applied to simultaneously fit both spectra, using the same parameter set. In this manner, the electronic and ionic conductivity of the material as well as the area-specific resistance of the surface reaction and the chemical capacitance can be determined on a single microelectrode in a $\text{H}_2\text{-H}_2\text{O}$ atmosphere. The applicability of this new tool was demonstrated in $\text{SrTi}_{0.7}\text{Fe}_{0.3}\text{O}_{3-\delta}$ (STFO) thin film microelectrodes, deposited on single-crystalline yttria-stabilized zirconia (YSZ) substrates. All materials parameters that contribute to the polarization resistance of STFO electrodes in a reducing atmosphere could thus be quantified.

Received 4th June 2014,
Accepted 3rd September 2014

DOI: 10.1039/c4cp02467b

www.rsc.org/pccp

1 Introduction

Mixed ionic and electronic conducting (MIEC) perovskite-type oxides may be applied in cathodes of intermediate temperature solid oxide fuel cells (SOFCs) and are widely investigated as porous or thin film electrodes.^{1–3} Some of these materials have high chemical stability also under reducing conditions, which makes them potential candidates for SOFC anodes. Mixed conducting anodes may help solving some problems of the generally employed Ni-YSZ composite anodes, such as carbon deposition, sulfur-poisoning and redox cycling stability.^{2,4} Several studies on porous perovskite anodes (*e.g.* $(\text{La}_{0.75}\text{Sr}_{0.25})(\text{Cr}_{0.5}\text{Mn}_{0.5})\text{O}_{3-\delta}$ (LSCM)^{5–7}), or cermet anodes involving perovskite-type and ceria-based mixed conductors^{6,8,9} were carried out and partly revealed low area specific resistances.

However, the perovskite-type materials were mostly studied as porous anodes and mechanistic interpretation of the impedance spectra is therefore complicated due to the complex and ill-defined geometry (*e.g.* effective surface area) and current paths. Thin film model electrodes offer well-defined geometry and

surface area, simple charge transport paths and good reproducibility, making them a very useful tool for the investigation of fundamental reaction mechanisms. This was extensively shown for cathode materials,^{10–14} but mechanistic electrochemical studies on mixed conducting thin film anodes are only available for ceria-based materials.⁹ Recently, also mechanistic studies of the anodic surface reaction of doped and undoped ceria were performed using ambient pressure XPS.^{15–17}

When acceptor-doped mixed conductors are used as SOFC anodes rather than cathodes, not only the surface reaction changes, but also some crucial bulk parameters such as electronic and ionic conductivity may change by orders of magnitude. Owing to the low chemical potential of oxygen in $\text{H}_2\text{-H}_2\text{O}$ atmospheres, especially the electronic p-type conductivity significantly decreases. Accordingly, not only the surface reaction and ionic charge transport, but also electronic conduction may be rate limiting in the reducing atmosphere. This further complicates the interpretation of conventional impedance studies on such anodes, even for thin film electrodes. For example, moderate electronic conductivity (in the order of 1 S cm^{-1}) may lead to medium-frequency features in the impedance spectra for electrodes without additional current collectors,¹⁸ whereas in the case of much lower electronic conductivity a current collector

Institute of Chemical Technologies and Analytics, Vienna University of Technology, Getreidemarkt 9, 1060 Vienna, Austria. E-mail: andreas.nenning@tuwien.ac.at

is mandatory. In ref. 9, the electronic and ionic conductivity of ceria films were measured by a method which however requires the film to be an excellent ionic conductor and to exhibit an electrolytic conductivity domain. The relevance of electronic and ionic charge transport in MIEC electrodes was also confirmed by numerical simulations.^{19,20} In this contribution, we introduce a novel approach for an impedance spectroscopic analysis of thin film electrodes with significant resistive contributions not only from the surface reaction but also from charge transport processes in the electrode bulk and thus for typical mixed conducting anode materials. Two interdigitating metallic current collectors are placed in one thin film microelectrode. This allows an in-plane impedance measurement between these two current collectors as well as a “classical” measurement *versus* an extended counter-electrode. In this manner we obtain two complementary impedance spectra on one and the same electrode. For both measurement modes, equivalent circuit models are developed. Those can be used for simultaneous fitting of both acquired spectra with the same parameter set. Using this technique, electronic and ionic conductivity as well as the area specific resistance of the surface reaction and the chemical capacitance can be quantified on a single microelectrode.

This novel method is demonstrated to be applicable to $\text{SrTi}_{0.7}\text{Fe}_{0.3}\text{O}_{3-\delta}$ electrodes in a $\text{H}_2\text{-H}_2\text{O}$ atmosphere. This oxide was already investigated as a cathode material, revealing a highly catalytic surface in an oxygen atmosphere.^{21,22} Also mechanistic studies have been carried out for the cathodic oxygen reduction,^{22,23} but detailed studies on the performance as a fuel cell anode and investigation of the electrochemical reactions and defect chemistry in a $\text{H}_2\text{-H}_2\text{O}$ atmosphere have not been carried out so far.

2 Experimental details and measurement modes

2.1 Sample preparation and electrode design

Pulsed laser deposition (PLD) was used to produce dense thin films of $\text{SrTi}_{0.7}\text{Fe}_{0.3}\text{O}_{3-\delta}$ (STFO) with a thickness ranging from 103 to 310 nm on single-crystalline yttria-stabilized zirconia (YSZ) with 9.5 mol% Y_2O_3 . The YSZ substrates had a size of $10 \times 10 \times 0.5 \text{ mm}^3$ and [100] surface orientation. Thin films were deposited at a substrate temperature of $610 \pm 10 \text{ }^\circ\text{C}$ in 0.02 mbar oxygen. The deposition time was varied between 16.6 minutes (3000 pulses) and 50 minutes (9000 pulses) with the laser operating at a pulse energy of 400 mJ (at the laser) and a repetition rate of 3 Hz. Prior to the STFO deposition, a micro-structured platinum thin film was employed as an electronic current collector (Fig. 1a). For comparison, Pt current collectors were also deposited on top of the STFO layer (Fig. 2b). The platinum layer (100 nm thickness) was sputter deposited and micro-structured by photolithography and ion beam etching. To increase the stability of the Pt films, 5 nm of titanium were employed as an adhesion layer. SEM imaging indicated dense and flat films of STFO grown on YSZ and on platinum (see Fig. 2b). θ - 2θ diffraction patterns measured on a Bruker D8 GADDS indicate single phase, [110] oriented thin films grown on YSZ (see Fig. 2b).

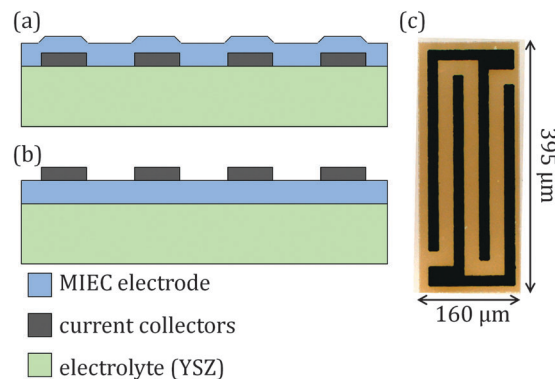


Fig. 1 Schematic cross-section of an electrode with a current collector beneath (a) and on top (b) of the MIEC film. Optical microscope picture of an electrode used in this study (c).

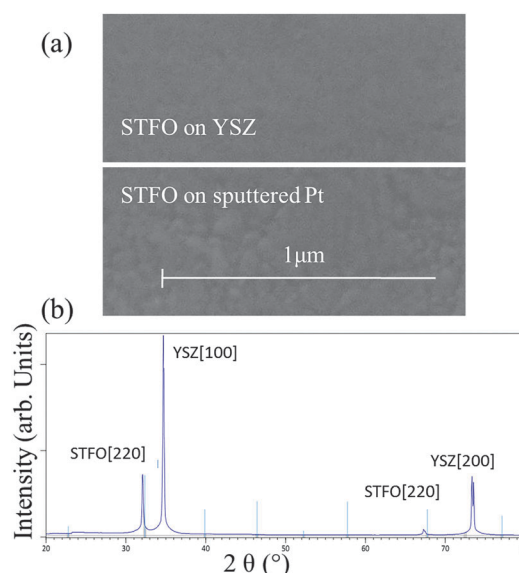


Fig. 2 SEM image of the STFO surface (a); top: film grown on YSZ, bottom: film grown on Pt. Diffraction pattern of the film (b).

Other orientations were not observed. Breaking edge images of the film indicate a thickness of $310 \pm 10 \text{ nm}$ for the film deposited with 9000 pulses (0.034 nm per pulse). After deposition of the STFO films and current collectors, rectangular microelectrodes with a size of $160 \times 395 \text{ } \mu\text{m}^2$ were produced by means of photolithography and ion beam etching.

The geometry of the electrode and current collectors is displayed in Fig. 3, and a microscopic picture is given in Fig. 1c. Three different geometries for the current collectors with varying finger distance were used on the same substrate and the exact measures are given in Table 1.

2.2 Contacting modes and impedance measurements

The two current collectors in each microelectrode reduce the impact of the electronic sheet resistance. Nevertheless, the resistances caused by charge transport processes may still be

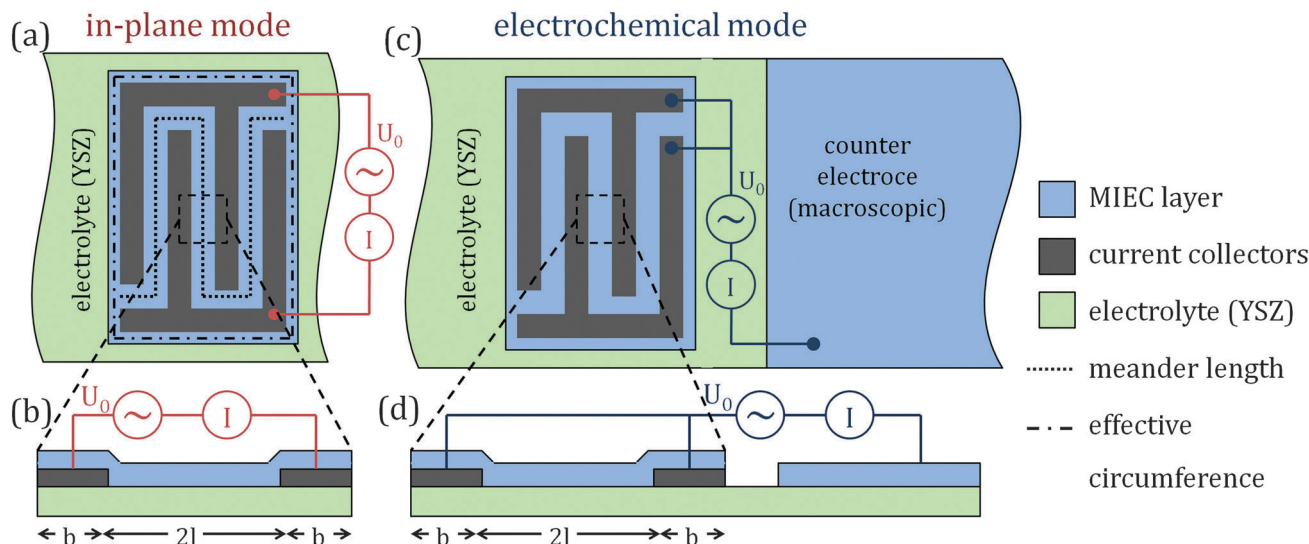


Fig. 3 Top view (a, c) and cross-section (b, d) of the two measurement modes. In the in-plane mode (a, b) the voltage is applied between the two metal finger structures. In the electrochemical mode (c, d), both current collectors are treated as one electrical terminal and measured against a macroscopic counter-electrode.

Table 1 Dimensions of the electrodes and current collectors. The meander length and effective circumference are as shown in Fig. 3a

| No. of metal fingers | Finger distance ($2l$) (μm) | Finger width ($2b$) (μm) | Meander length (μm) | Effective circumference (μm) | MIEC dimensions (μm^2) |
|----------------------|--|---|----------------------------------|---|-------------------------------------|
| 4 | 5 | 15 | 2625 | 1090 | 160×395 |
| 6 | 11.7 | 15 | 1840 | 1052 | 160×395 |
| 8 | 25 | 15 | 1160 | 985 | 160×395 |

relevant compared to the resistance of the surface reaction (depending on the exact geometry, temperature and atmospheric conditions). In order to separate resistive contributions of transport processes from those of the surface reaction, each microelectrode contains two interdigitating Pt current collectors. By two different contact configurations two measurement modes can be realized. This is displayed in Fig. 3 in top view and cross section. In the in-plane measurement (Fig. 3a and b), the impedance is measured between the two metal finger structures. In the electrochemical mode (Fig. 3c and d) both current collectors are electrically treated as one terminal. The impedance is then measured against the macroscopic counter electrode of the same material, also containing a Pt current collector. This is the measurement mode which is usually applied for electrochemical characterization of microelectrodes. Owing to the much larger counter electrode, the impedance in the electrochemical mode is almost entirely determined by the microelectrode and the electrolyte.¹⁰

These two measurement modes on one and the same electrode are the basis of the present study. In the following we derive equivalent circuits describing the corresponding impedance measurements and explain why fitting of both modes enables the simultaneous determination of all relevant resistive and capacitive materials parameters of the system, *i.e.* ionic conductivity, electronic conductivity, area-specific resistance

of the surface reaction and interfacial resistance as well as the chemical capacitance.

The STFO electrodes were investigated using this novel technique in a H_2 - H_2O atmosphere and consistency of the analysis was confirmed by geometry variations (see Section 4). Piezoelectric high-precision actuators (Newport Agilis) were employed to contact the current collectors in the electrodes *via* gold-plated steel tips with a tip radius of 1–3 μm . Details of the measurement stage are given in ref. 24. The impedance spectra were acquired using a Novocontrol Alpha-A High Performance Frequency Analyser, equipped with a Novocontrol POT/GAL 30 V/2 A interface, in the frequency range of 0.01 Hz to 1 MHz at an AC amplitude of 10 mV RMS. The measurements were carried out at temperatures between 490 and 800 $^\circ\text{C}$ in an atmosphere of 2.5% H_2 and about 2.5% H_2O vapor in argon as a carrier gas.

3 Equivalent circuit models for thin film electrodes with current collectors

3.1 Transmission line circuit model for transport losses in thin film electrodes

For a meaningful interpretation of the impedance measurements in both measurement modes, a thorough discussion of the polarization and charge transport processes within mixed conducting thin film electrodes with current collectors is required. In Fig. 4, the possible reaction paths for anodic current flow are shown. In a H_2 - H_2O atmosphere, the main resistive contributions are typically the hydrogen oxidation on the surface of the MIEC layer as well as electronic and ionic in-plane charge transport within the thin film. Additionally, also a spreading resistance in the electrolyte and an ionic interface resistance at the electrolyte-MIEC interface have to be considered; these turned out to be comparatively small in the case of STFO.

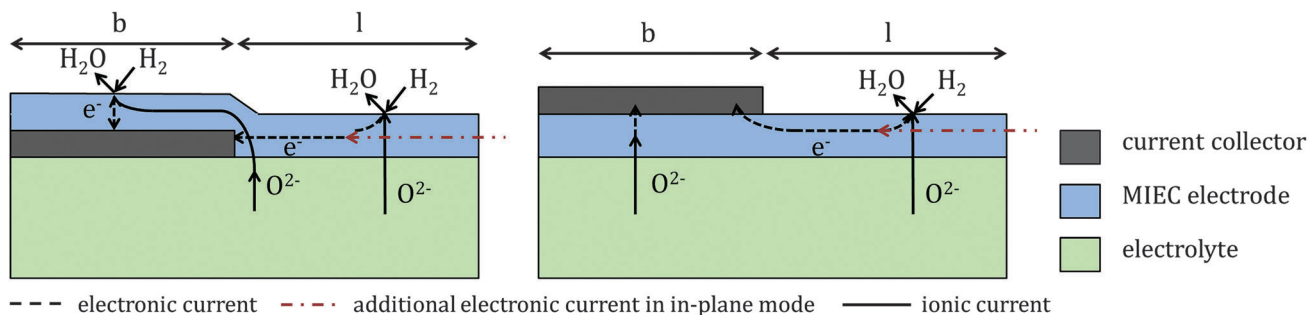


Fig. 4 Processes relevant for the impedance of a MIEC anode with metal fingers below the anode (left) and on top (right). Arrows indicate anodic current, although impedance spectroscopy probes both directions.

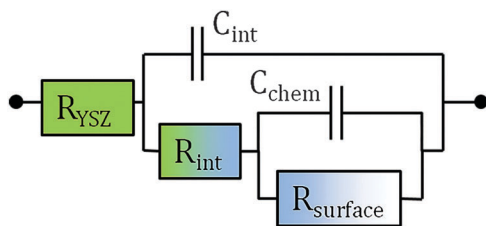


Fig. 5 Equivalent circuit for MIEC electrodes with high electronic and ionic conductivity, according to ref. 12 and 25.

As a starting point, the impedance response of MIEC electrodes with very high electronic and ionic conductivity and rate limiting surface kinetics will be discussed. For such electrodes, all ionic and electronic in-plane and across-plane charge transport processes are without resistance. According to ref. 12 and 25 the equivalent circuit consists of a resistive offset caused by the electrolyte (R_{YSZ}) and an electrode part containing the resistance related to the surface reaction (R_{surface}) in parallel with the chemical capacitance of the MIEC bulk (C_{chem}). If the ionic transport across the electrode–YSZ interface causes an additional resistive contribution, an interfacial resistance and capacitance (R_{int} and C_{int}) have to be added, as depicted in Fig. 5. Also in cases where in-plane charge transport losses become relevant, this circuit will play a central role.

As a next step we consider a thin film electrode with moderate or low electronic and ionic conductivity. It was shown by Jamnik and Maier that for one-dimensional systems the impedance of the MIEC bulk is described by a transmission line circuit.²⁵

In our case, one-dimensionality is not given since in-plane as well as across-plane currents are important. However, still the concept of a transmission line, reflecting the electrochemical potentials and the transport of electrons and oxygen ions, is applicable. This is shown in the following.

The geometry of our thin film electrodes (Fig. 3) is characterized by a very large ratio between film thickness (100–300 nm) and lateral finger distance or width (5–25 μm), *i.e.* an aspect ratio in the order of 1 : 100. Moreover, the MIEC film is either in electric contact with an excellent electron conductor (current collector) or a fast ion conductor (YSZ). The combination of these two facts allows us to define a “fast” and a “slow” carrier. Those are not distinguished by their specific conductivities in the MIEC. Rather, the “fast” carrier can easily move either in the current

collector (electrons) or in the electrolyte (ions) and therefore its electrochemical potential is laterally homogeneous in the “fast” phase. Hence, only across-plane transport of this “fast” carrier has to be considered in the MIEC. On the other hand, for the “slow” carrier in-plane distances are much larger than across-plane distances and therefore only in-plane variations of its electrochemical potential in the MIEC are relevant.

Owing to this lateral variation, the driving force for oxygen exchange (and stoichiometric polarization) becomes inhomogeneous along the electrode. This can be quantified by a local “polarization potential” (η^*), which reflects the driving force of across-plane currents of “fast” carriers and the surface reaction. The dimension of η^* is Volt, although it cannot be related to an electrostatic potential step. In the simplest case of lossless lateral current within the electrode it is position independent and equals the applied voltage, see Appendix A.1.

For in-plane transport losses (of the “slow” carrier), but lossless across-plane charge transport of the “fast” carrier (in the MIEC and across interfaces), the polarization potential is simply the local driving force of the surface reaction. It correlates with the change of the local chemical potential of oxygen in the electrode $\Delta\mu_{\text{O}}^{\text{ode}}$ due to an applied bias *via*

$$\eta^* = \frac{\Delta\mu_{\text{O}}^{\text{ode}}}{2F} = \frac{\Delta\tilde{\mu}_{\text{ion}}^{\text{ode}} - 2\Delta\tilde{\mu}_{\text{eon}}^{\text{ode}}}{2F} \quad (1)$$

The symbols $\tilde{\mu}_{\text{ion}}^{\text{ode}}$ and $\tilde{\mu}_{\text{eon}}^{\text{ode}}$ denote electrochemical potentials of oxygen ions and electrons in the MIEC, respectively; Δ indicates the difference in the equilibrium value without applied bias. Therefore $\Delta\mu_{\text{O}}^{\text{ode}}$ is also the difference in the chemical potential of oxygen between the atmosphere and the polarized electrode. It varies in-plane in a polarized MIEC electrode.

When across-plane charge transport losses of the “fast” carrier within the MIEC or across an interface are relevant, the polarization potential has to be defined in a more general manner. For the MIEC layer on top of the electrolyte and thus ions being “fast” carriers it is given by

$$\eta^{*\text{yte}} = \frac{\Delta\tilde{\mu}_{\text{ion}}^{\text{yte}} - 2\Delta\tilde{\mu}_{\text{eon}}^{\text{ode}}}{2F} \quad (2)$$

In contrast to eqn (1), the electrochemical potential of oxygen ions is now located in the electrolyte and $\eta^{*\text{yte}}$ formally reflects the overall driving force of the reaction $\text{H}_2\text{O} + 2\text{e}_{\text{ode}}^- \rightarrow \text{H}_2 + \text{O}_{\text{yte}}^{2-}$.

It corresponds to the sum of kinetic losses of the surface reaction, the according across-plane ionic current within the MIEC and the ion transfer at the MIEC–electrolyte interface.

For a MIEC on top of the current collector, electrons are the “fast” and ions the “slow” carrier. The polarization potential can then be defined as

$$\eta^{*metal} = \frac{\Delta\tilde{\mu}_{ion}^{ode} - 2\Delta\tilde{\mu}_{con}^{metal}}{2F} \quad (3)$$

Here, the electrochemical potential of electrons is located in the metal. Therefore, η^{*metal} corresponds to the overall driving force of both, surface reaction and electronic across-plane current within the MIEC (and if relevant across a Schottky barrier at the MIEC–current collector interface). Therefore it is the driving force of the reaction $H_2O + 2e_{metal}^- \rightarrow H_2 + O_{ode}^{2-}$. For an electrode geometry consisting of long and thin metal fingers, the local polarization potential only depends on the distance from the metal fingers.

In the following, it is explained on an argumentative level that the one-dimensional generalized transmission line circuits given in Fig. 6 can describe such a system. In Appendixes A.2 and A.3 the impedance functions of these circuits are derived from the rate laws of charge transport and reactions for mixed conducting thin films. However, the following equivalent circuits are graphical and more intuitive representations of these equations.

In-plane transport of the “slow” charge carrier can be quantified by the sheet resistance elements (R_{eon} or R_{ion}). The “fast” charge carrier moves either in a good electronic or a good ionic conductor and therefore has laterally homogeneous electrochemical potential in the “fast” phase, irrespective of its conductivity in the MIEC. This is treated by a short circuit in its transport rail of the equivalent circuit. The element Y_{ap} describes the (area-specific) across-plane admittance and is related to surface reaction and transport of the “fast” carrier. Y_{ap} also includes charging and discharging of the chemical capacitance as well as possible interfacial resistances. More specific circuits for this element will be introduced later. Defining this element as an admittance allows a mathematically consistent discretization into small (or infinitesimal) elements. In Fig. 6 the resulting circuits for a MIEC on the electrolyte (Fig. 6a) and on the current collector (Fig. 6b) are shown. Also a symbolic representation of the transmission lines (r.h.s.) is given, which will be used in the following. The l.h.s. terms in Fig. 6 emphasize that the driving forces for the in-plane and across-plane currents are determined by the electrochemical potentials of ions and electrons as given in eqn (2) and (3).

The impedance of such a transmission line depends on the left- and right-hand side termination. When a thin film MIEC electrode with current collectors is described by such a circuit, the edges of the metal fingers are appropriate locations of the terminals. For negligible losses in the electrolyte and counter

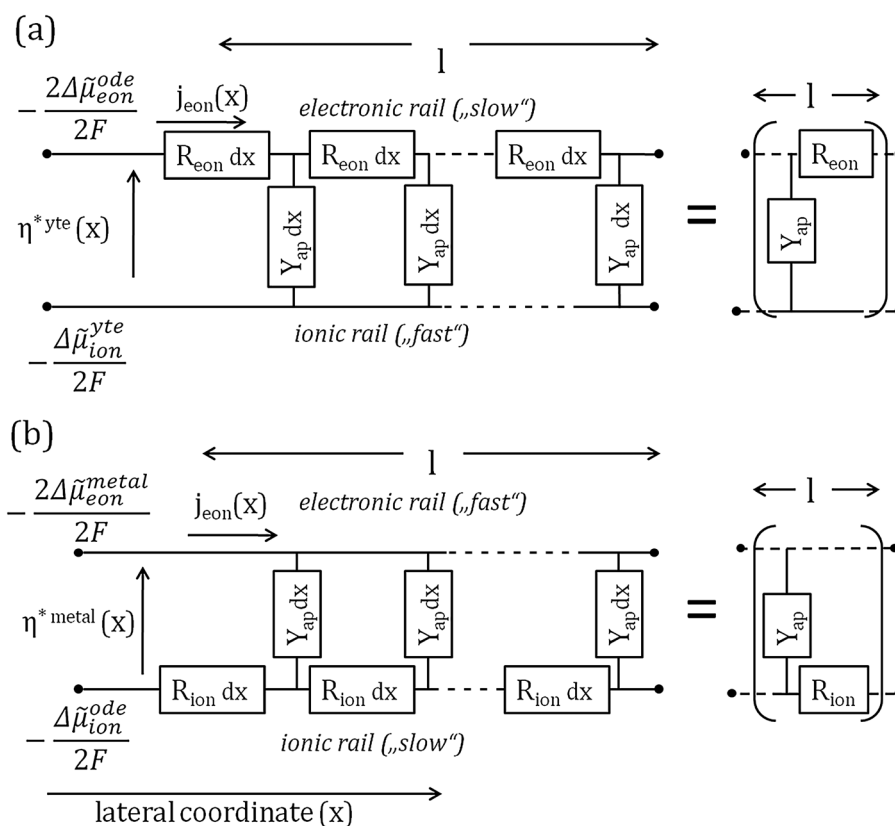


Fig. 6 Generalized transmission line circuit describing a MIEC thin film on an electrolyte (a). Generalized transmission line circuit describing a MIEC film on an electronic conductor (e.g. current collector) (b).

electrode, the polarization potential at these points equals the applied voltage, which is either $+U_0$ or $-U_0$, depending on the finger and measurement mode.

3.2 Application of the generalized transmission line circuit to MIEC electrodes with interdigitating current collectors

In this section, we specify the equivalent circuits for the MIEC electrodes used in this study. Those electrodes consist of two regions with different electrochemical properties: the region of the current collectors and the free MIEC area (electrode grown on YSZ without current collectors). The circuit of the free MIEC area does not depend on the location of the current collectors (above or beneath the MIEC layer), whereas this location does play an important role in the region of the current collectors. The circuits are very similar for electrochemical and in-plane measurement and differ only at the terminal parts. Still, the impedance spectra for both modes are very different. Cross-plane charge transport of electrons is assumed to be lossless in all cases.

3.2.1 Free MIEC area. A mixed conducting thin film on an ionic conductor can be modeled by the transmission line circuit displayed in Fig. 6a. The element R_{eon} represents the electronic sheet resistance ($R_{\text{eon}} = \rho_{\text{eon}}/d$) with ρ_{eon} and d being the electronic resistivity and film thickness, respectively. The cross-plane admittance (element Y_{ap} of the circuit) reflects ionic cross-plane charge transport resistances and oxygen exchange *via* the surface reaction and the chemical capacitance. In our STFO electrodes, ionic cross-plane charge transport within the MIEC is almost lossless, while a small resistance at the STFO–YSZ interface could be observed. Consequently, the element Y_{ap} can be specified by the simplified equivalent circuit shown in Fig. 5 (without YSZ resistance).

The terminals of the transmission line are at the edges of the metal fingers, see Fig. 7a. At the edges of the metal fingers the electrochemical potential of electrons is defined by the current collector, and the electrochemical potential of oxygen ions remains at its equilibrium value when neglecting the electrolyte resistance. Consequently, in the electrochemical measurement mode (Fig. 3c and d), the polarization potential of the left and right hand side terminal is the applied voltage $+U_0$, see Appendix A1. The electrolyte resistance will be introduced

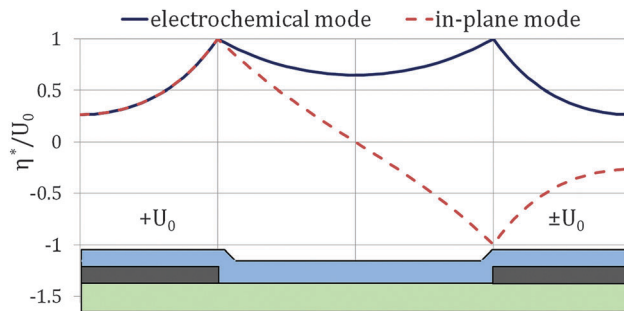


Fig. 8 Calculated normalized polarization potential (η^*/U_0) in the DC case for in-plane and electrochemical measurement modes. The circuit parameters are equal to the simulated spectra in Section 3.4.

later as a terminal part. In the in-plane mode (Fig. 3a and b), the left and right-hand side terminals are oppositely polarized with $+U_0$ and $-U_0$, respectively. This situation is shown in Fig. 7a. These conditions can also be described by simpler circuits that use only one voltage source: The electrochemical mode is equal to an open end terminal in the center of the transmission line (Fig. 7b), and the in-plane mode corresponds to a short circuit in the center of the transmission line (Fig. 7c). This equivalence becomes clear when calculating the in-plane distribution of the polarization potential for both measurement modes, which is plotted in Fig. 8. The calculation also includes the transmission line above the current collectors. In the electrochemical mode, the gradient of η^* is zero in the center between the metal fingers (equal to an open end boundary). In the in-plane mode, η^* is zero in the center (equal to a short circuit). The corresponding equations are derived in the Appendixes A.3.2 and A.3.3. In the following circuits, the representation involving only one voltage source will be used, meaning that only half of the metal finger distance (l) is considered in the circuit. The resulting transmission line for the free surface area is part of the final circuits in Fig. 9 and 10.

3.2.2 Region beneath the current collector. One possible realization of the electrode has metallic current collectors on top of the MIEC film (shown in Fig. 4, r.h.s.). Beneath the metal, the MIEC is conductively connected with the electrolyte

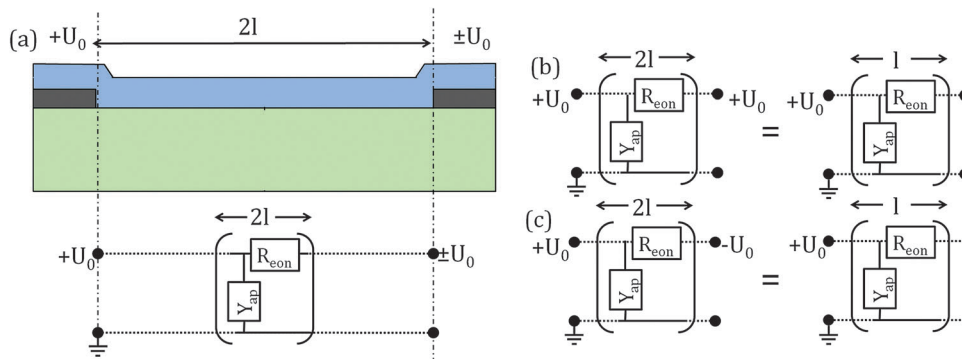


Fig. 7 Terminals of the transmission line circuit which are set to the metal finger edges (a). For the electrochemical measurement mode (b), two circuits with different given boundary conditions result in the same impedance function. The same is true for the in-plane measurement mode (c).

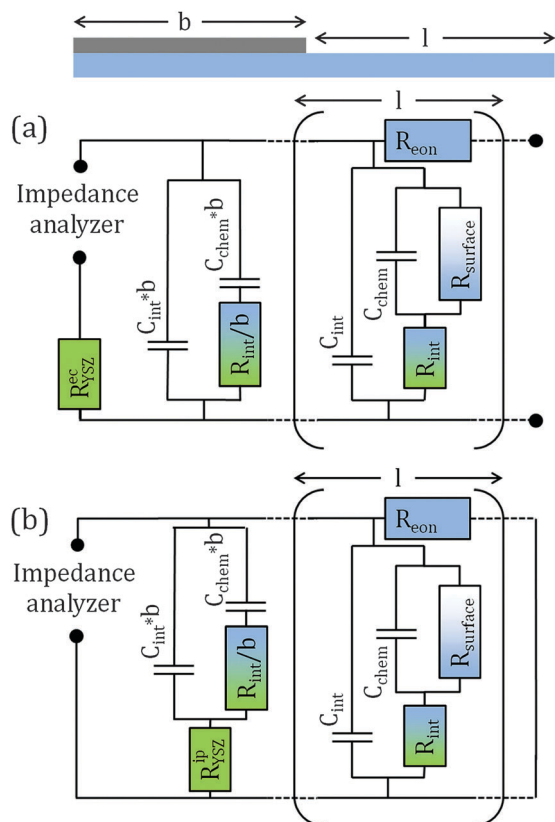


Fig. 9 Equivalent circuit for an electrode with a current collector on top: (a) electrochemical mode, (b) in-plane mode. The elements R_{int} , C_{int} , C_{chem} and R_{surface} reflect area-specific resistances and capacitances, R_{eon} is the electronic sheet resistance.

and with an electronic conductor, therefore both charge carriers can be treated as “fast” carriers. Accordingly, relevant ionic as well as electronic charge transport within the MIEC layer only occurs across-plane, so only the ionic STFO–YSZ interface resistance has to be considered for charge transport. The surface reaction, on the other hand, is blocked by the dense platinum layer. Consequently, a well suited model for this region is the simplified equivalent circuit in Fig. 5 (without YSZ resistance) with $R_{\text{surface}} \rightarrow \infty$. The resulting circuit is the l.h.s. part of the circuits in Fig. 9.

3.2.3 Region above the current collector. The MIEC region above the current collector exhibits a homogeneous electrochemical potential of electrons and can be modeled by the transmission line circuit in Fig. 6b. R_{ion} stands for the ionic sheet resistance ($R_{\text{ion}} = \rho_{\text{ion}}/d$), with ρ_{ion} being the ionic resistivity of the film on top of the current collector. The across-plane admittance Y_{ap} can be described by a parallel connection of the chemical capacitance C_{chem} and surface resistance R_{surface} , provided an electronic interface resistance between MIEC and current collector is negligible. Due to the different microstructure of the MIEC on YSZ and metal, also R_{surface} and C_{chem} might be different on these two substrates. In the case of our STFO electrodes, strong differences could be excluded by geometry variations, see Section 4.2. Therefore, these parameters are set to be equal for the MIEC on YSZ and on the current collector.

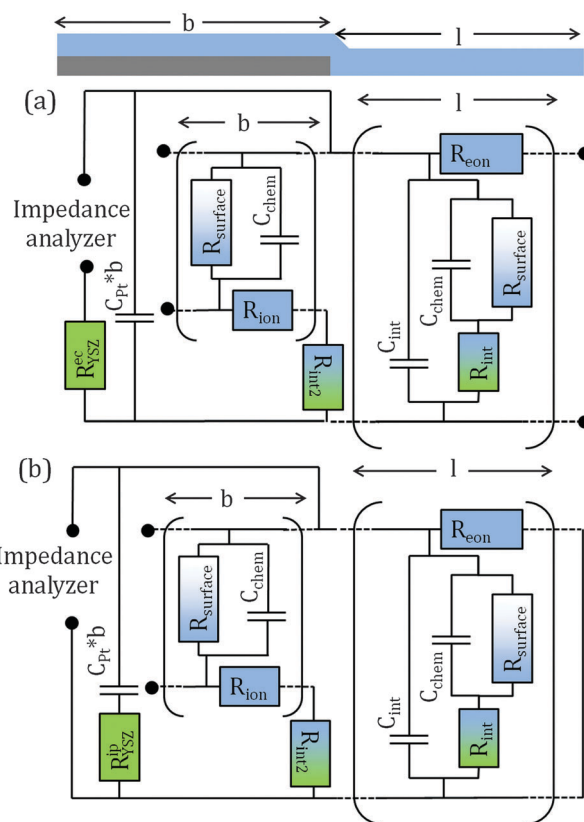


Fig. 10 Equivalent circuit for an electrode deposited on top of the current collectors: (a) electrochemical mode, (b) in-plane mode. The elements R_{int} , C_{int} , C_{chem} and R_{surface} reflect area-specific resistances and capacitances, R_{eon} and R_{ion} are electronic and ionic sheet resistance, respectively.

Also for this transmission-line circuit, potentials at the terminals have to be defined. At the edges of the metal fingers oxygen ions are exchanged between MIEC and electrolyte. Here, the ionic MIEC–electrolyte interface resistance has to be considered as a terminal part of the transmission line. If this interface resistance is small compared to the total resistance, the terminal can be approximated by $R_{\text{int}2} = \sqrt{R_{\text{int}}R_{\text{ion}}}$ (see Appendix A.3.4). Also a capacitance at the current-collector|YSZ interface is likely to be relevant,²⁶ this is represented by the C_{pt} element which is placed in parallel to the transmission line. The resulting circuit is the left-hand side transmission line in Fig. 10. Owing to symmetry reasons, the polarization potential at the two edges of a metal finger is equal. Equivalent to this symmetrical terminal polarization, the transmission line can also be terminated with an open end in the center of the metal finger. This termination is appropriate for both modes. Accordingly, only half of the metal finger width (b) is considered in the equivalent circuit.

3.2.4 Electrolyte resistance. Owing to the different current paths, the magnitude of the electrolyte resistance is very different in the electrochemical and in-plane mode and is treated differently in in-plane and electrochemical measurement modes. In the electrochemical mode, the entire measured current has to pass the electrolyte. Therefore, the electrolyte causes a simple resistive offset in this case (the element $R_{\text{YSZ}}^{\text{ec}}$ in the final circuit – Fig. 9a and 10a).

In the DC-case of the in-plane mode, a pure electronic current path is possible with the electrolyte not playing any role. In the high frequency regime, however, ionic current in the electrolyte between two adjacent metal fingers may become relevant for the impedance. This ionic current is capacitively coupled to the current collecting fingers. An exact description would require numerical methods. For the absolute resistive contribution of the electrolyte being small compared to the in-plane DC resistance, which is the case for anodes with moderate or low electronic conductivity, an approximation can be made. The electrolyte resistance is placed in series to the capacitively coupled current path between the metal fingers (the element R_{YSZ}^{ip} in the final circuit – Fig. 9b and 10b) – so it causes a resistive offset in the high-frequency regime and plays no role in the DC-case. If the electronic sheet resistance is very high (exceeding the condition in eqn (5)), there will also be a DC ionic in-plane current in the electrolyte. However, in this case, the DC resistance of the in-plane mode will be orders of magnitude larger than the electrolyte resistance.

The final equivalent circuits for in-plane and electrochemical modes differ in only two points: The right-hand side boundary of the free electrode transmission line is either an open end or a short circuit and the electrolyte resistance is treated differently. The according analytic impedance functions are given in the Appendix A.4.

3.3 Fitting routine

Given the rather complex circuits, concerns regarding over-parametrisation may arise. This may indeed be a problem when only one measurement mode is used for fitting of experimental results. However, the derived equivalent circuits are valid for in-plane and electrochemical measurement on one and the same electrode and therefore include identical materials parameters. Both acquired impedance spectra can thus be simultaneously fitted with a single parameter set by minimizing the sum of squared relative errors for both spectra. Such a simultaneous fit of two different measurements strongly increases the significance of the fitting parameters in terms of accuracy and mechanistic interpretation, compared to the fitting of only one spectrum. This dual fit is key for being able to accurately deduce all relevant resistive and capacitive parameters which contribute to the electrode impedance. In-plane electronic and ionic charge transport affects the spectra of the electrochemical mode in a very similar manner, but has very different consequences in the in-plane mode. Before running the fitting routine, the measured impedance spectra have to be corrected for the electrode geometry. For the electrochemical mode, the spectra are normalized to the total circumference of both metal fingers. In the in-plane mode, the impedance is normalized to the meander length between the fingers (see Fig. 3b). At the borders of the mixed conducting electrode, the in-plane current density is zero, irrespective of the used measurement mode. This condition is equivalent to the electrochemical measurement mode. Accordingly, also the in-plane measurement includes a (small) contribution which corresponds to the circuit of the electrochemical measurement mode, caused by the open

end boundary condition at the MIEC border. Since this contribution is proportional to the effective circumference of the MIEC layer (Fig. 3a), an according proportion of the current measured in the electrochemical mode has to be subtracted from the in-plane measurement. This is done even though the effect is rather small. After normalization to the metal finger circumference, the impedance has the unit of $\Omega \text{ cm}$, such as the circuit model. The fitting parameters reflect area-specific capacitances and resistances for across-plane current (R_{surface} , R_{int} , C_{chem} , C_{Pt} , C_{int}) and the electronic and ionic sheet resistance for the in-plane current (R_{eon} and R_{ion}). Only the electrolyte resistances of both modes are not corrected for geometry. However, after a calibration (comparison with circular electrodes), they can be used to determine the ionic conductivity of the substrate. From a known conductivity–temperature relationship the electrode temperature can then be calculated.²⁷

3.4 Simulated spectra for current collectors above and beneath the electrode

The shape and size of impedance spectra is typically very different for in-plane and electrochemical modes and also strongly depends on the placement of the current collector and of course on the corresponding materials parameters. Examples of simulated spectra are shown in Fig. 11. Typical values obtained in Section 4 have been chosen for the main resistive, capacitive and geometric parameters (surface area-specific resistance (ASR): $100 \Omega \text{ cm}^2$, electronic resistivity: $200 \Omega \text{ cm}$, ionic resistivity: $2000 \Omega \text{ cm}$, chemical capacitance: 5 mF cm^{-2} , film thickness: 100 nm , metal finger width and distance: $20 \mu\text{m}$). Electrolyte as well as interfacial resistances and capacitances were set to 0 since they deliver only minor contributions to the impedance spectra considered in this study. The most obvious difference caused by the placement of the metal layer is a smaller DC resistance when the current collectors are beneath the electrode, which is caused by a larger area exposed to the atmosphere.

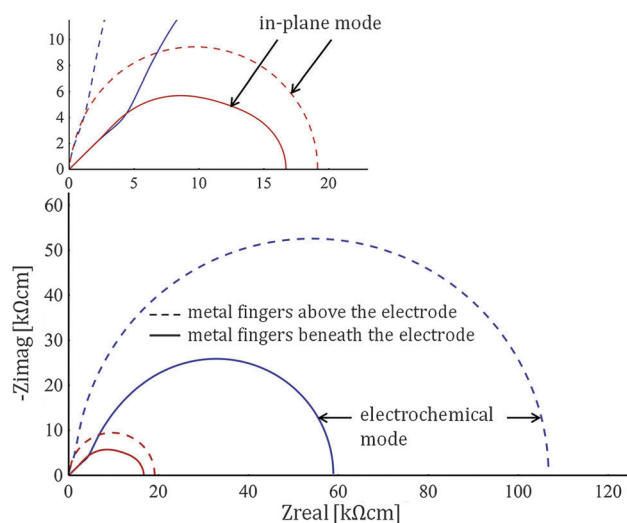


Fig. 11 Simulated spectra for current collectors on top (dashed lines) and beneath the electrode (solid lines). The inset shows a magnification of the in-plane spectra.

Also these spectra exhibit more features. This was also experimentally confirmed (not shown) and indicates that this configuration is advantageous when aiming at the determination of all relevant electrochemical properties. For electrodes with metal fingers on top, the large chemical capacitance of the part covered by the current collectors is measured in parallel to the transmission line circuit of the free surface region. This parallel circuit disguises the Warburg-like impedance that is typically observed for transmission lines in the high-frequency range. Furthermore, the ionic conductivity is not relevant in the corresponding circuit model and thus not available. Also, the platinum current collectors may be catalytically active when placed on top of the MIEC, which might further complicate the analysis. In the experiments shown in the following, only electrodes deposited above the metal fingers have therefore been used. According to the circuit model, the electronic conductivity is measured in-plane above the YSZ substrate, while the ionic conductivity is measured in-plane above the current collector.

4 Experimental results and discussion

The suggested method for investigating mixed conducting electrodes in a reducing atmosphere was applied to $\text{SrTi}_{0.7}\text{Fe}_{0.3}\text{O}_{3-\delta}$ electrodes deposited on top of platinum current collectors (*cf.* Section 2). In the following, we first show measured impedance spectra and discuss the origin of the different features. Then, the consistency of the new method is demonstrated by variations of the electrode geometry. Finally, information on the temperature dependence of the materials parameters is given.

4.1 Frequency dependence of the electrode polarization

Fig. 12a displays the in-plane and electrochemical impedance spectra after normalization, measured at 660 °C with a finger distance of 11.7 μm and a STFO film thickness of 103 nm. Both spectra reveal several impedance features, partly semicircle-like and partly with 45° slopes in the Nyquist plot. The circuits derived in Section 3 were used to simultaneously fit both spectra.

Nine parameters are considered in the equivalent circuits (R_{surface} , R_{int} , C_{chem} , C_{Pt} , C_{int} , R_{eon} , R_{ion} , $R_{\text{YSZ}}^{\text{ec}}$ and $R_{\text{YSZ}}^{\text{ip}}$). In order to increase the numerical stability of the fitting routine, the electrolyte resistances ($R_{\text{YSZ}}^{\text{ec}}$, $R_{\text{YSZ}}^{\text{ip}}$) were determined from the resistive offset in the high-frequency region of the two measurement modes and set as fixed values during the fitting routine. Also the capacitance of the Pt-Ti-YSZ (C_{Pt}) interface was found to be too large for a reliable determination of the STFO-YSZ interface capacitance, *cf.* C_{int} could therefore not be fitted and was fixed to 0 in the fitting routine. Hence, only six independent parameters were used to fit both spectra. (R_{surface} , R_{int} , C_{chem} , C_{Pt} , R_{eon} , R_{ion}).

The Nyquist plots in Fig. 12a also show fit lines that demonstrate the fit accuracy. In order to understand the mechanisms causing the shape of both spectra, the fit parameters and the circuit models were used to calculate the amplitude of the local polarization potential as a function of position and frequency.

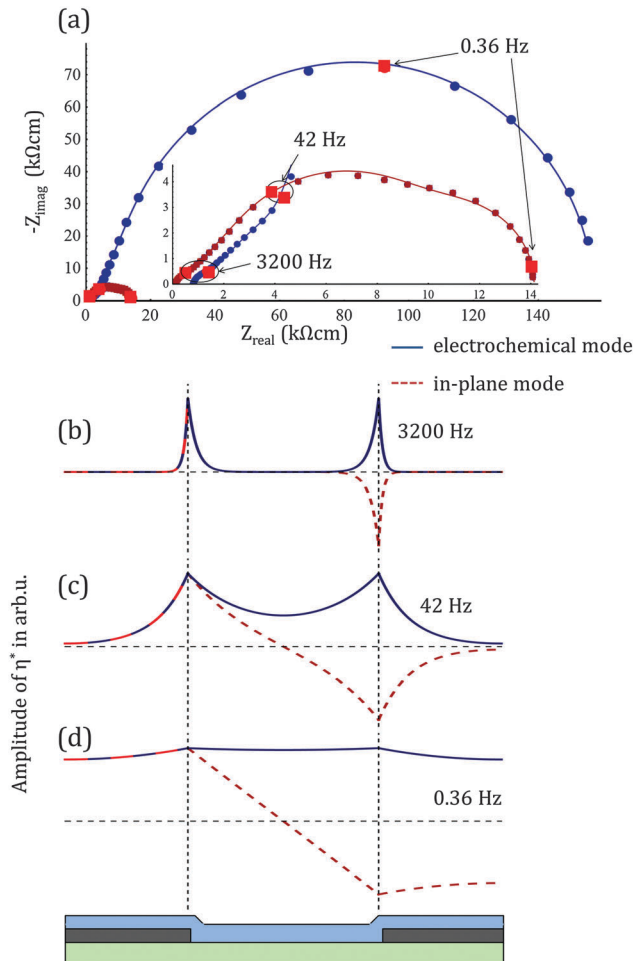


Fig. 12 (a) Measured (symbols) and fitted (lines) impedance spectra of an electrode with 103 nm thickness and 11.6 μm finger distance at 660 °C. (b–d) The calculated lateral distribution of the polarization potential is plotted for three different frequencies.

From this, an important conclusion can be drawn: The fraction of the electrode area which is polarized strongly depends on the frequency, as shown in Fig. 12b–d. This is understandable on a qualitative level: At high frequencies (*e.g.* measurement at 3200 Hz, Fig. 12b), oxygen exchange in the film is possible *via* charging and discharging of the chemical capacitance. Compared to this process, electronic and ionic in-plane charge transport exhibits comparatively high resistance. This results in a short attenuation length of the polarization potential. The impedance response of electrochemical and in-plane measurement in this frequency range is very similar (except for the electrolyte offset) and is mainly determined by the chemical capacitance and the electronic conductivity. At lower frequencies, the impedance of the chemical capacitance increases and the attenuation length becomes larger. For attenuation lengths comparable to or larger than the finger distance, the spectra of the two measurement modes become very different (below 42 Hz in Fig. 12). The slightly asymmetric shape of the low-frequency semicircle in the electrochemical mode as well as the small low-frequency semicircle in the in-plane measurement

(between 42 and 0.36 Hz) are related to the resistance of the in-plane current of oxygen ions on top of the current collectors.

For near-DC conditions oxygen exchange in the MIEC occurs primarily *via* the surface reaction, which is rate-limiting for the STFO electrodes used in this study. Therefore the polarization is nearly homogeneous along the electrode in the electrochemical mode. Accordingly, the main contribution to the DC-resistance of the electrochemical measurement is the surface reaction. For in-plane measurements, the polarization potential varies linearly and the DC-resistance is mainly given by the electronic sheet resistance. However, for a large distance between the current collector fingers or very low electronic conductivity, the attenuation length of the electrode polarization may be similar to or smaller than the finger distance in near-DC conditions. In this case, both spectra become very similar in shape and size (after normalization) and electron transport as well as oxygen exchange contribute to both spectra in the same way. This was also confirmed experimentally at lower temperature (not shown).

4.2 Geometry variations

The derived equivalent circuits are applicable to electrodes of different thickness and metal finger distance. The size and shape of the spectra changes with geometry, but the deduced materials parameters should stay the same. In order to prove this, a sample with a 103 nm thick STFO film was prepared. Three different electrode geometries were realized on this sample. The width of the metal fingers was kept constant at 15 μm and the metal finger distance was varied between 5, 11.6 and 25 μm . Fig. 13 depicts typical impedance spectra including the fit for these three metal finger distances. The quality of the fits is very good, given that there are only six independent parameters for the fit of two impedance spectra. The parameters determined for different geometries at a constant temperature of 660 $^{\circ}\text{C}$ are summarized in Fig. 14. Three different electrodes were measured and averaged for each finger distance.

Although some parameters (surface ASR and ionic resistivity) exhibit substantial scatter even for nominally identical electrodes and thus partly large error bars, the fitted materials parameters are independent of the exact electrode geometry. The accurate fit of the measurements, combined with the independence of the fitting parameters on the metal finger distance, strongly suggests the validity of the model and the appropriateness of the method. Also the error of the fitting routine for one electrode is smaller than the corresponding standard deviation found for geometrically identical microelectrodes, on one sample.

The measurements were repeated for a three times thicker film (310 nm) and they confirmed the consistency in terms of finger distance variation. The results of both film thicknesses are summarized in Table 2, averaged over all finger distances.

Many parameters (chemical capacitance, electronic resistivity and area-specific resistance (ASR) of the ionic interface) only slightly depend on the film thickness, however, some parameters show significant trends. The capacitance of the Pt-Ti-YSZ interface is considerably smaller for the 310 nm film. Moreover, the

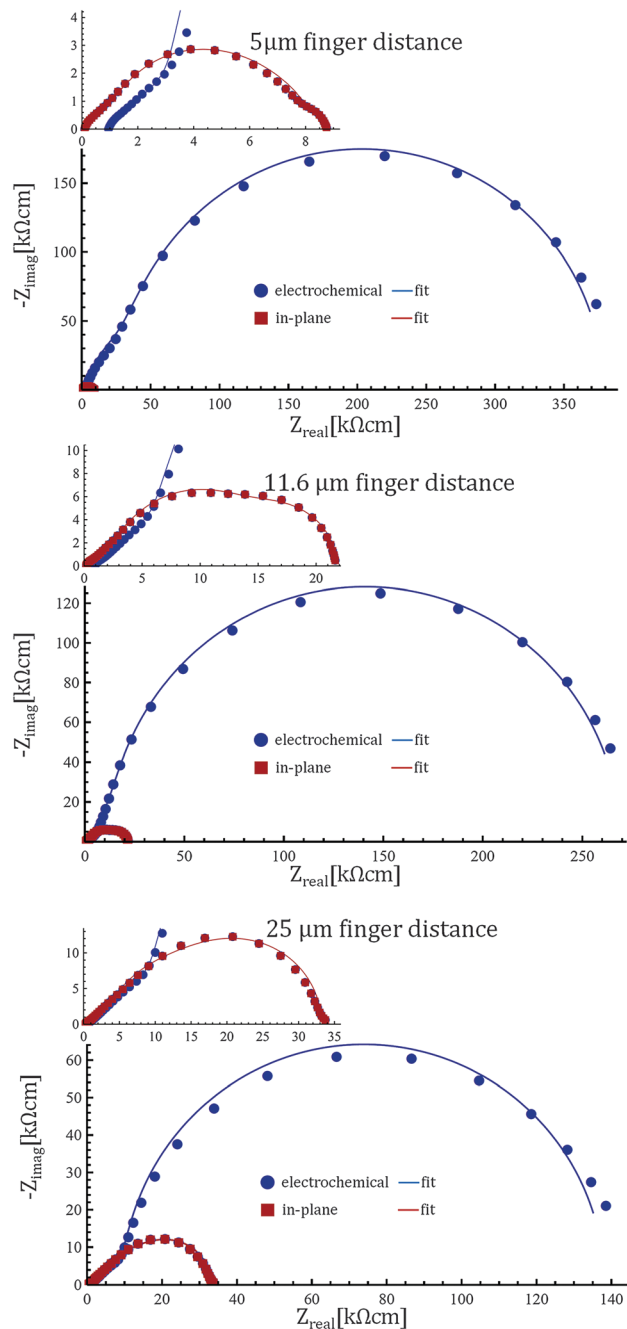


Fig. 13 Impedance spectra (symbols) including fit (lines) for a 103 nm thick STFO microelectrode with different finger distances at 660 $^{\circ}\text{C}$. The insets show magnifications emphasising the in-plane measurements.

surface ASR is larger for the 103 nm film, but even nominally identical thin films exhibited similar scatter for this parameter. The (in-plane) ionic resistivity of the 310 nm film is significantly smaller. The electronic and ionic conductivity of the thicker film are in reasonable agreement with values measured on sintered pellets of similarly doped $(\text{Sr}_{1-x}\text{Fe}_x)\text{TiO}_3$.^{28,29} Further investigations are required to understand the reasons behind the different ionic resistivity of the two films. For example, a thickness dependent microstructure might be the origin of the higher lateral ionic

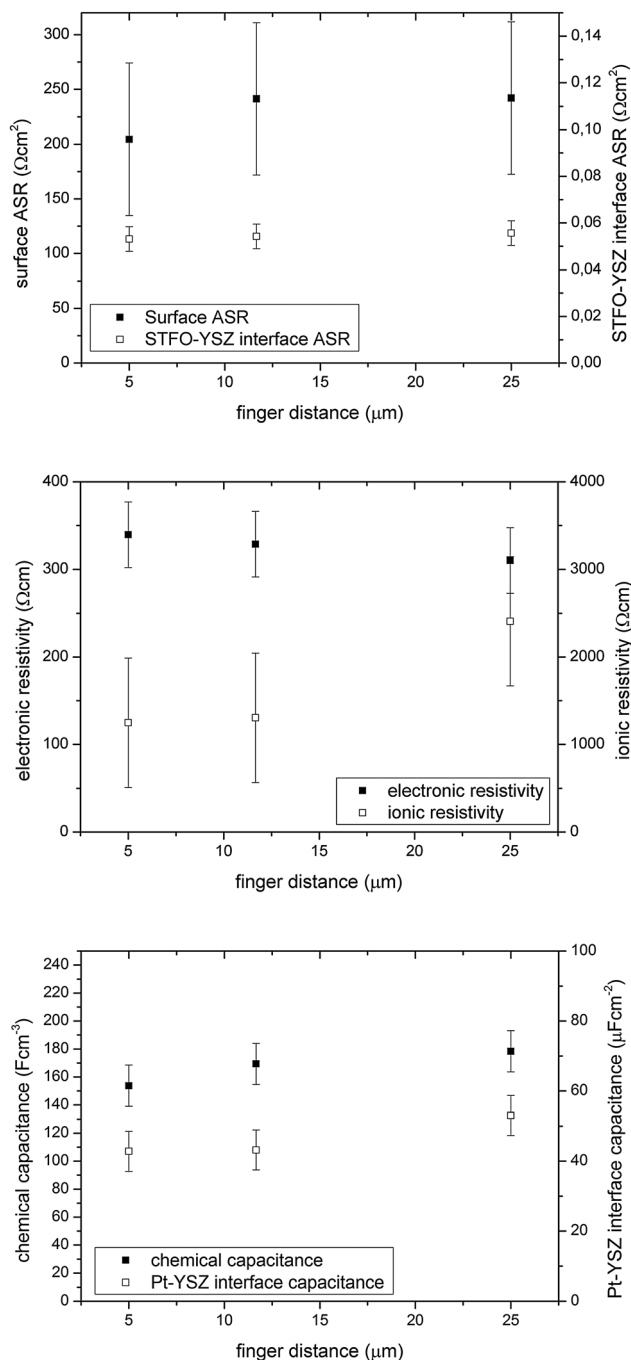


Fig. 14 Materials parameters of different electrodes at 660 ± 10 °C with a film thickness of 103 nm, deduced by fitting of the impedance spectra. The parameters are independent of the metal finger distance (ASR = area specific resistance).

resistivity of the thinner film. In-plane tracer diffusion experiments could reveal further information on ionic transport properties but those are far from trivial to perform on thin films.^{30–32} Moreover, four-point conductivity measurements³³ would be helpful as cross-check experiments but those require deposition of the films on an insulating substrate, which might affect the results. However, variation of the current collector geometry on the same thin film revealed consistent results in all fitting parameters.

4.3 Temperature dependence

All relevant resistive materials parameters of STFO anodes are thermally activated. The determination of these activation energies provides valuable information for both application and mechanistic interpretation. Even though it is not the scope of this paper to perform a detailed study of these temperature dependences and their defect chemical interpretation, first results can be given and some activation energies can be estimated.

The activation energies of the different resistive parameters are listed in Table 3. A constant activation energy in the investigated temperature range can be observed for electronic and ionic resistivity. Interestingly, the electronic and ionic resistivity differs by less than one order of magnitude. The chemical capacitance and interfacial capacitance (not shown) are also temperature-dependent, but not Arrhenius-type thermally activated. The increase of the chemical capacitance with increasing temperature probably reflects the increasing concentration of electronic and/or ionic defects. The surface reaction exhibits a rather low activation energy at low temperatures (< 610 °C), which increases strongly at elevated temperature. Such a result might be explained by two parallel reaction paths. However, also time-dependent changes of R_{surface} were observed (activation with increasing temperature and degradation when again decreasing the temperature). The Arrhenius plot in Fig. 15 therefore reflects both, temperature and time-dependent changes of the surface kinetics. Further investigations on this phenomenon are necessary for a detailed understanding.

4.4 Possibilities and restrictions

The novel method introduced in this paper is expected to be applicable to a wide variety of mixed conductors, especially for materials with high electronic sheet resistance. However, if certain parameters are either very large or very small, the impedance response of the electrodes becomes insensitive to them. The most important value in this respect is the characteristic attenuation length of the polarization potential (l_a) in the DC-case, which is related to the resistances of in-plane current and the surface reaction. It is given by

$$l_a = \sqrt{\frac{R_{\text{surface}}}{R_{\text{sheet}}}}, \quad (4)$$

with R_{sheet} being the ionic (R_{ion}) or electronic (R_{eon}) sheet resistance. If this length is much smaller than half of the metal finger distance, the center between the metal fingers is unpolarized in both measurement modes. Then the (geometry-corrected) impedance spectra for electrochemical and in-plane measurement become very similar and the fitting error strongly increases. For a reliable quantification of the ionic resistivity, the attenuation length above the metal fingers has to be larger than half of the metal finger width. For a typical thin film electrode with fine structured current collectors (thickness: 200 nm, finger width and distance: 5 μm), this leads to an upper limit of both electronic and ionic resistivity:

$$\rho[\Omega \text{ cm}] < 320 \text{ cm}^{-1} \times R_{\text{surface}}[\Omega \text{ cm}^2] \quad (5)$$

Table 2 Mean values of the fitting parameters and their standard deviation for two different thin film samples at 660 °C

| Electrode property | 103 nm film | 310 nm film |
|--|-------------------|-------------------|
| Chemical capacitance ($F\text{ cm}^{-3}$) | 167 ± 13 | 160 ± 16 |
| Surface ASR ($\Omega\text{ cm}^2$) | 229 ± 62 | 137 ± 42 |
| STFO–YSZ interface ASR ($\Omega\text{ cm}^2$) | 0.054 ± 0.005 | 0.055 ± 0.007 |
| Pt–Ti–YSZ interface capacitance ($\mu F\text{ cm}^{-2}$) | 46 ± 5 | 25 ± 3 |
| Ionic resistivity ($\Omega\text{ cm}$) | 1650 ± 656 | 395 ± 105 |
| Electronic resistivity | 326 ± 33 | 291 ± 70 |

Table 3 Activation energies of the resistive parameters, 310 nm film

| Resistive property | Activation energy (eV) |
|----------------------------------|------------------------|
| Electronic conductivity | 1.2 ± 0.1 |
| Ionic conductivity | 1.3 ± 0.1 |
| Surface ASR, $T < 610\text{ °C}$ | 0.7 ± 0.2 |
| Surface ASR, $T > 610\text{ °C}$ | 1.6 ± 0.2 |
| Ionic interface ASR | 1.2 ± 0.2 |

For the electronic resistivity, there are also lower boundaries: if the DC resistance of the in-plane measurement is comparable to or smaller than the corresponding electrolyte resistance, there exists no analytical model for the impedance response of the in-plane measurement. In this case, only its DC-value can be used to determine the electronic resistivity, but a simultaneous fit of two spectra is no longer possible. If the electronic conductivity is very high, which is the case for many mixed conducting cathodes in air ($\gg 1\text{ S cm}^{-1}$), the resistance of the current collectors or a possible Schottky barrier between MIEC and metal (which was neglected so far) may become similar or even larger than the sheet resistance. In such a case, a large separation of the current collectors or a 4-point measurement that eliminates possible contact resistances (*e.g.* Van der Pauw method³³) is required for the determination of the electronic sheet resistance. Accordingly our novel approach is not considered to be a replacement of established methods, but rather a helpful complementary tool to investigate mixed conductors with properties typically occurring in a reducing atmosphere.

5 Conclusions

Many mixed conducting oxide materials exhibit low electronic conductivity when placed in a reducing atmosphere. Therefore, electronic and ionic charge transport as well as the electrochemical surface reaction can cause significant resistive contributions that lead to complex impedance spectra even for geometrically simple thin film electrodes. We developed a novel design of thin film microelectrodes with two interdigitating current collectors per electrode. This configuration enables two different measurement modes on one and the same microelectrode: an in-plane mode where the voltage is applied between both current collectors on one electrode and a conventional electrochemical measurement *versus* a macroscopic counter-electrode. An appropriate impedance model was developed for both measurement modes, based on two transmission lines representing a mixed conducting thin film either in contact with the current collector or the electrolyte. Both acquired impedance spectra can be simultaneously fitted to these equivalent circuits using a single parameter set. Hence, all relevant resistive and capacitive contributions can be quantified and a possible overparametrization of the model is avoided. A more detailed analysis showed that the polarization potential, which is related to the local chemical potential of oxygen, varies laterally in the mixed conductor. This variation strongly depends on the measurement mode as well as the frequency. This method was successfully employed to $\text{SrTi}_{0.7}\text{Fe}_{0.3}\text{O}_{3-\delta}$ anodes, where electronic and ionic conductivity, ASR of the surface reaction, chemical capacitance and the resistance of the electrode–electrolyte

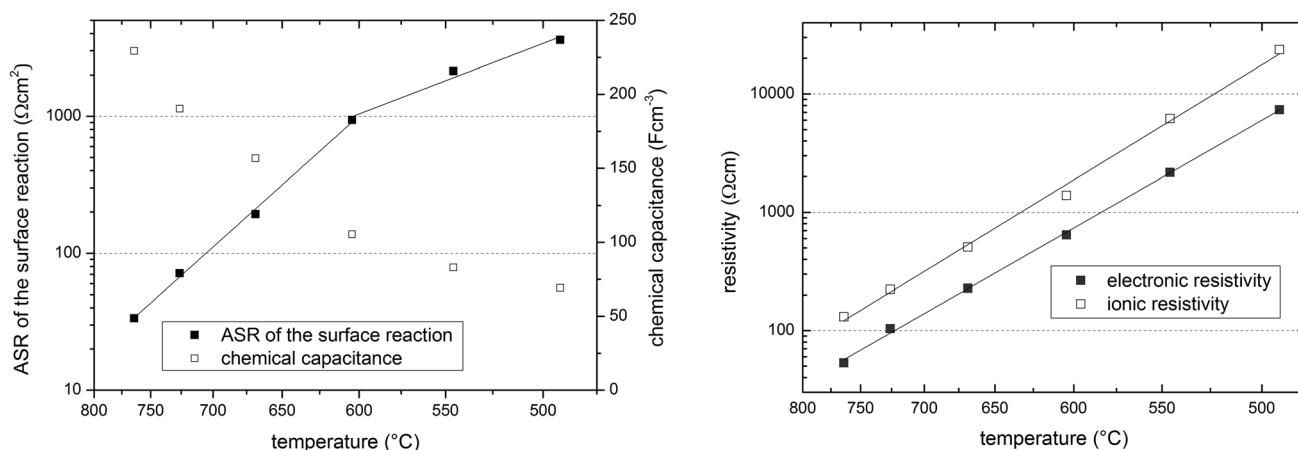


Fig. 15 Arrhenius plot of the relevant resistive parameters and plot of the chemical capacitance between 490 and 760 °C.

interface could be determined on a single thin film electrode with comparatively small experimental effort. However, it was also shown that this approach is only applicable for a limited parameter range in terms of ionic and electronic conductivity. Acceptor-doped mixed conductors in a reducing atmosphere are often within this parameter range and our method is expected to be particularly helpful for analyzing such materials.

A Appendix

A.1 Polarization of a mixed conducting electrode without transport losses

As a starting point, the polarization of a mixed conducting microelectrode (working electrode) with rate limiting surface kinetics and negligible losses in the electrolyte is briefly discussed. When neglecting resistive losses in the electrolyte and counter-electrode, the electrochemical potential of oxygen ions ($\tilde{\mu}_{\text{ion}}$) remains unchanged in the working electrode, counter electrode and electrolyte, ($\Delta\tilde{\mu}_{\text{ion}} = 0$). The electrochemical potential of electrons in the working electrode is defined by the voltage applied to the current collector ($\Delta\tilde{\mu}_{\text{e-con}}^{\text{ode}} = -FU_0$). Consequently, the chemical potential of oxygen in the electrode ($\Delta\mu_{\text{O}}^{\text{ode}}$) is given as

$$\Delta\mu_{\text{O}}^{\text{ode}} = \Delta\tilde{\mu}_{\text{ion}}^{\text{ode}} - 2\Delta\tilde{\mu}_{\text{e-con}}^{\text{ode}} = 2FU_0. \quad (\text{A.1})$$

Therefore the polarization potential η^* (eqn (1)) equals the applied voltage U_0 .

A.2 Relation between polarization potential and current

When charge transport losses in a thin film MIEC play a significant role, the polarization potential (η^*) also varies in-plane. For a thin film MIEC on either an electronic or an ionic conductor, a direct relation between in-plane currents and polarization potential can be established. The electric current density j_k of a charge carrier k with charge number z_k is proportional to the gradient of its electrochemical potential and conductivity σ_k . For gradients only along the in-plane coordinate of a MIEC film, this can be expressed as

$$j_k = -\frac{d\tilde{\mu}_k}{dx} \frac{1}{z_k F \rho_k}. \quad (\text{A.2})$$

(i) For a MIEC on an ionic conductor, the polarization potential was defined as (see eqn (2))

$$\eta^{\text{yte}} = \frac{\Delta\tilde{\mu}_{\text{ion}}^{\text{yte}} - 2\Delta\tilde{\mu}_{\text{e-con}}^{\text{ode}}}{2F}. \quad (\text{A.3})$$

The electrochemical potential of ions in the electrolyte is assumed to be laterally homogeneous due to its high ionic conductivity and much larger thickness compared to the MIEC film. Differentiating eqn (A.3) with respect to the spatial coordinate (x) and combining it with eqn (A.2), one obtains

$$\frac{d}{dx} \eta^{\text{yte}}(x) = \frac{d}{dx} \frac{-\tilde{\mu}_{\text{e-con}}^{\text{ode}}(x)}{F} \quad (\text{A.4})$$

$$\frac{d}{dx} \eta^{\text{yte}}(x) = -j_{\text{con}} \rho_{\text{e-con}}. \quad (\text{A.5})$$

Only the current density integrated along the film thickness (d) is measurable and can be related to the electronic sheet resistance ($R_{\text{e-con}}$). When assuming homogeneous electronic conductivity within the entire film, eqn (A.5) transfers to

$$\frac{d}{dx} \eta^{\text{yte}}(x) = -I_{\text{con}} R_{\text{e-con}} \quad (\text{A.6})$$

with

$$R_{\text{e-con}} = \frac{\rho_{\text{e-con}}}{d} \quad (\text{A.7})$$

And the current per electrode length

$$I_{\text{con}} = dj_{\text{e-con}}. \quad (\text{A.8})$$

(ii) For a MIEC film on an electronic conductor, the polarization potential was defined as (see eqn (3)):

$$\eta^{\text{metal}} = \frac{\Delta\tilde{\mu}_{\text{ion}}^{\text{ode}} - 2\Delta\tilde{\mu}_{\text{e-con}}^{\text{metal}}}{2F}. \quad (\text{A.9})$$

This expression can be differentiated with respect to the spatial coordinate and combined with eqn (A.2):

$$\frac{d}{dx} \eta^{\text{metal}}(x) = \frac{d}{dx} \frac{\tilde{\mu}_{\text{ion}}^{\text{ode}}(x)}{2F} \quad (\text{A.10})$$

$$\frac{d}{dx} \eta^{\text{metal}}(x) = j_{\text{ion}} \rho_{\text{ion}}. \quad (\text{A.11})$$

Analogous to the case discussed above, we obtain

$$\frac{d}{dx} \eta^{\text{metal}}(x) = I_{\text{ion}} R_{\text{ion}}, \quad (\text{A.12})$$

$$R_{\text{ion}} = \frac{\rho_{\text{ion}}}{d}, \quad (\text{A.13})$$

$$I_{\text{ion}} = j_{\text{ion}} d. \quad (\text{A.14})$$

R_{ion} is the ionic sheet resistance. The different signs in eqn (A.16) and (A.12) indicate that electronic current (in technical direction) is directed towards lower polarization potential, while ionic current is directed towards higher polarization potential. This result may seem confusing, but the polarization potential does not reflect an electrostatic potential. Rather it can be related to the chemical potential of oxygen (see eqn (1)) and different flux directions are well known from chemical diffusion (see ref. 34, chapter 6.3.3).

A.3 Impedance of the generalized transmission lines

A.3.1 General solution. The generalized transmission line circuits in Fig. 6 are applicable to thin films in which transport losses occur in only one spatial direction, and the electrochemical potential of the “fast” charge carrier is homogeneous in its fast phase. This is the case for our electrodes with a thin film MIEC being deposited either on an ionic or an electronic conductor. In impedance measurements, the current at the terminals of the electronic rail is measured. For a MIEC on the current collector

it is therefore appropriate to consider the electronic current in the current collector rather than the ionic current in the MIEC. The electronic current is exactly opposite to the ionic one ($I_{\text{eon}}(x) = -I_{\text{ion}}(x)$), as visible in the circuit model in Fig. 7b and c). Hence, a single equation can describe charge transport in both situations, MIEC on the current collector and MIEC on the electrolyte. It reads

$$\frac{d}{dx}\eta^* = -R_{\text{sheet}}I_{\text{con}}(x) \quad (\text{A.15})$$

and represents eqn (A.12) and (A.16). The sheet resistance R_{sheet} is either electronic (for MIEC on electrolyte) or ionic (for MIEC on metal). Apart from its influence on in-plane charge transport, the polarization potential is also the driving force of across-plane currents and the surface reaction. The relation between polarization potential, in-plane currents and across-plane currents can be quantified by a one dimensional continuity equation

$$\frac{d}{dx}I_{\text{con}} = -Y_{\text{ap}}\eta^*(x). \quad (\text{A.16})$$

The source term $Y_{\text{ap}}\eta^*$ describes the local across-plane current density of the polarization-driven electrochemical reactions (e.g. surface reaction and charging of the chemical capacitance). The across-plane admittance Y_{ap} is here treated on a black-box level, it is adopted to certain situations in Section 3.2. Eqn (A.15) and (A.16) result from the laws of charge transport and reactions that are driven by the local polarization potential, without the use of an equivalent circuit. The generalized transmission line circuit is therefore a graphical representation of these processes that can be described by equivalent equations.

The two equations describing the generalized transmission line can be combined by differentiating eqn (A.15) and we obtain

$$\frac{d^2}{dx^2}\eta^*(x) = -R_{\text{sheet}}\frac{d}{dx}I_{\text{con}}(x) = R_{\text{sheet}}Y_{\text{ap}}\eta^*(x). \quad (\text{A.17})$$

With an exponential ansatz, the general solution can be found.

$$\eta^*(x) = Ae^{\gamma x} + Be^{-\gamma x} \quad (\text{A.18})$$

$$I_{\text{con}}(x) = -\frac{A\gamma e^{\gamma x} - B\gamma e^{-\gamma x}}{R_{\text{sheet}}} \quad (\text{A.19})$$

$$\gamma = \sqrt{R_{\text{sheet}}Y_{\text{ap}}} \quad (\text{A.20})$$

The parameters A and B are determined by the polarization potentials of the left and right hand side terminal, which depend on the measurement mode. For our electrode design, the edges of the metal fingers are the boundaries of the transmission line. At these points, lateral electronic or ionic charge transport within the electrode is not required and the polarization potential for both transmission lines can be calculated as

$$\eta^* = U_0 - \eta_{\text{terminal}} \quad (\text{A.21})$$

η_{terminal} reflects the overpotential in the terminal parts caused by the circuit elements R_{int2} and R_{YSZ} in Fig. 9 and 10. Without loss of generality, $\eta_{\text{terminal}} = 0$ can be assumed in the following calculation of the transmission line impedance.

A.3.2 Symmetric terminal polarization. Symmetric terminal polarization means equal polarization potential on the left and right hand side of a generalized transmission line. This is the case for the free MIEC area in the electrochemical measurement mode. Also electrodes deposited on top of the metal fingers exhibit symmetrical terminal polarization for the MIEC above the current collector. For a transmission line with a length of $2l$ and $x = 0$ in the center between the terminals these conditions read:

$$\eta^*(-l) = U_0, \eta^*(l) = U_0. \quad (\text{A.22})$$

With these boundary conditions, eqn (A.18) can be solved as

$$\eta^*(x) = U_0 \times \frac{\cosh(\gamma x)}{\cosh(\gamma l)}. \quad (\text{A.23})$$

And the resulting in-plane current is given by

$$I_{\text{con}}(x) = \frac{U_0}{R_{\text{sheet}}} \times \frac{\sinh(\gamma x)}{\cosh(\gamma l)}. \quad (\text{A.24})$$

Eqn (A.24) exhibits zero in-plane current in the center ($I_{\text{con}}(0) = 0$). Therefore an open end terminal in the center of the transmission line is equal to symmetric boundary conditions, which is depicted in Fig. 7b.

In impedance spectroscopic measurements, the spatial distribution of current and potential remains on a black box level. Only the length-specific total impedance (Z) can be measured at the terminals. In the symmetrical case this is given by

$$Z_{\text{sym}} = \frac{\eta^*(-l)}{I(-l)} = \frac{R_{\text{sheet}}}{\gamma} \coth(\gamma l). \quad (\text{A.25})$$

A.3.3 Asymmetric terminal polarization. Asymmetric terminal polarization means opposite polarization of the left and right hand side terminals. This is found for the free surface area in the in-plane measurement mode and can be represented as

$$\eta^*(-l) = U_0, \eta^*(l) = -U_0. \quad (\text{A.26})$$

Under these boundary conditions, the solution of eqn (A.18) is given as

$$\eta^*(x) = U_0 \times \frac{\sinh(\gamma x)}{\sinh(\gamma l)}. \quad (\text{A.27})$$

In analogy to Section A.3.2, the measurable length-specific impedance in the asymmetric case is given as

$$Z_{\text{asym}} = \frac{\eta^*(-l)}{I(-l)} = \frac{R_{\text{sheet}}}{\gamma} \tanh(\gamma l). \quad (\text{A.28})$$

Eqn (A.27) exhibits zero polarization potential in the center ($\eta^*(0) = 0$), which is equal to a short-circuit terminal in the center, as depicted in Fig. 7c.

A.3.4 Infinite length boundary conditions. The characteristic attenuation length of η^* in a transmission line is $\text{real}(\gamma^{-1})$. Hence, $\text{real}(\gamma l)$ is the ratio between the lateral feature size of an electrode and the charge carrier diffusion length. When the attenuation length is much smaller than the lateral feature size ($\text{real}(\gamma l) \gg 1$), the impedance functions for symmetric and

asymmetric boundary conditions converge against the solution for an infinitely long transmission line. An example is the Gerischer impedance. We then obtain

$$\tanh(\gamma l) \approx \coth(\gamma l) \approx 1 | \text{real}(\gamma l) \gg 1. \quad (\text{A.29})$$

With this approximation, eqn (A.5) and (A.28) lead to

$$Z_{\text{inf}} = \sqrt{\frac{R_{\text{sheet}}}{Y_{\text{ap}}}}. \quad (\text{A.30})$$

This situation can be found in the high-frequency region of the impedance spectra of typical mixed conducting anodes (see Section 4.1). In the DC-case, infinite length boundary conditions occur in the case of very large separation of the metal fingers as well as for very low electronic conductivity.

The same approximation is also applicable to a special part of our system: When the electrode is deposited above the current collectors, the oxygen ions flowing in the region above the current collectors still have to pass the electrode–electrolyte interface, as shown in Fig. 4, left. This interfacial resistance has to be treated as a terminal part, which can be approximated by a transmission line consisting of the ionic sheet resistance R_{ion} and the MIEC–electrolyte interface resistance R_{int} . For typical parameters (small ionic interface resistance and moderate ion conduction) the attenuation length in this transmission line is small and infinite length boundary conditions are applicable. According to eqn (A.28), this can be expressed as

$$R_{\text{int}2} = \sqrt{R_{\text{ion}} R_{\text{int}}}. \quad (\text{A.31})$$

R_{int} is the area specific ionic resistance of the MIEC/electrolyte interface, R_{ion} is the ionic sheet resistance and $R_{\text{int}2}$ is the terminal resistance of the left hand side transmission line depicted in Fig. 10.

A.4 Analytic functions for electrochemical and in-plane impedance

The circuits derived in Section 3.2 can finally be expressed by analytical impedance functions, which were used for fitting and are given here. For a parallel circuit, the following abbreviation will be used: $Z1 \parallel Z2 = Z1Z2/(Z1 + Z2)$. The symbols have the meanings of the equivalent circuit elements in Fig. 9 and 10, ω is the angular frequency, b and l are half of the metal finger width and half of the metal finger distance, respectively.

A.4.1 MIEC above current collectors. The corresponding circuits are depicted in Fig. 10. Z_{free} and Z_{metal} are the inverse of the area specific across-plane admittance (Y_{ap}^{-1}) for the free MIEC area and above the current collector, respectively. The impedance of the electrochemical mode (Z_{ec}) is given as

$$Z_{\text{ec}} = R_{\text{YSZ}}^{\text{ec}} + \frac{1}{i\omega C_{\text{Pt}} \times b} \left\| \left(\sqrt{R_{\text{con}} Z_{\text{free}}} \times \coth \left(\sqrt{\frac{R_{\text{con}}}{Z_{\text{free}}}} \times l \right) \right) \right\| \left(\sqrt{R_{\text{ion}} Z_{\text{metal}}} \times \coth \left(\sqrt{\frac{R_{\text{ion}}}{Z_{\text{metal}}}} \times b \right) + \sqrt{R_{\text{int}} R_{\text{ion}}} \right) \quad (\text{A.32})$$

with

$$Z_{\text{free}} = \frac{1}{i\omega C_{\text{int}}} \left\| \left(R_{\text{int}} + \left(R_{\text{surface}} \left\| \frac{1}{i\omega C_{\text{chem}}} \right\| \right) \right) \right\| \quad (\text{A.33})$$

and

$$Z_{\text{metal}} = R_{\text{surface}} \left\| \frac{1}{i\omega C_{\text{chem}}} \right\|. \quad (\text{A.34})$$

The impedance of the in-plane (Z_{ip}) mode differs only in the treatment of the electrolyte resistance and in the boundary conditions for the free MIEC area (asymmetric boundary conditions lead to a hyperbolic tangent function in the corresponding transmission line impedance)

$$Z_{\text{ip}} = \left(R_{\text{YSZ}}^{\text{ip}} + \frac{1}{i\omega C_{\text{Pt}} \times b} \right) \left\| \left(\sqrt{R_{\text{con}} Z_{\text{free}}} \times \coth \left(\sqrt{\frac{R_{\text{con}}}{Z_{\text{free}}}} \times l \right) \right) \right\| \left(\sqrt{R_{\text{ion}} Z_{\text{metal}}} \times \tanh \left(\sqrt{\frac{R_{\text{ion}}}{Z_{\text{metal}}}} \times b \right) + \sqrt{R_{\text{int}} R_{\text{ion}}} \right). \quad (\text{A.35})$$

A.4.2 MIEC beneath current collectors. The impedance of the circuit in Fig. 9 in the electrochemical mode (Z_{ec}) is given as

$$Z_{\text{ec}} = R_{\text{YSZ}}^{\text{ec}} + \sqrt{R_{\text{con}} Z_{\text{free}}} \times \coth \left(\sqrt{\frac{R_{\text{con}}}{Z_{\text{free}}}} \times l \right) \left\| \frac{1}{b} \times \left(\frac{1}{i\omega C_{\text{int}}} \left\| \left(R_{\text{int}} + \frac{1}{i\omega C_{\text{chem}}} \right) \right\| \right) \right\|. \quad (\text{A.36})$$

Z_{free} is in accordance with eqn (A.32). Also here, the impedance of the in-plane mode (Z_{ip}) differs only in the treatment of the electrolyte resistance and in the boundary conditions of the free MIEC area, which is expressed as

$$Z_{\text{ip}} = \sqrt{R_{\text{con}} Z_{\text{free}}} \times \tanh \left(\sqrt{\frac{R_{\text{con}}}{Z_{\text{free}}}} \times l \right) \left\| \left(\left(R_{\text{YSZ}}^{\text{ip}} \right) + \frac{1}{b} \times \left(\frac{1}{i\omega C_{\text{int}}} \left\| \left(R_{\text{int}} + \frac{1}{i\omega C_{\text{chem}}} \right) \right\| \right) \right) \right\|. \quad (\text{A.37})$$

Acknowledgements

The authors gratefully acknowledge funding by the Austrian Science Fund (FWF) projects no. F4509-N16 and no. W1243-N16.

References

- 1 S. B. Adler, *Chem. Rev.*, 2004, **104**, 4791–4844.
- 2 N. Q. Minh, C. Singhal and M. Williams, *ECS Trans.*, 2009, **17**, 211–219.
- 3 R. Merkle and J. Maier, *Angew. Chem., Int. Ed.*, 2008, **47**, 3874–3894.
- 4 P. I. Cowin, C. T. Petit, R. Lan, J. T. Irvine and S. Tao, *Adv. Energy Mater.*, 2011, **1**, 314–332.

- 5 S. Tao and J. T. S. Irvine, *J. Electrochem. Soc.*, 2004, **151**, A252–A259.
- 6 X. J. Chen, Q. L. Liu, S. H. Chan, N. P. Brandon and K. A. Khor, *Fuel Cells Bull.*, 2007, **2007**, 12–16.
- 7 S. Tao and J. T. S. Irvine, *Nat. Mater.*, 2003, **2**, 320–323.
- 8 S. Cho, D. E. Fowler, E. C. Miller, J. S. Cronin, K. R. Poepplmeier and S. A. Barnett, *Energy Environ. Sci.*, 2013, **6**, 1850–1857.
- 9 W. C. Chueh, Y. Hao, W. Jung and S. M. Haile, *Nat. Mater.*, 2012, **11**, 155–161.
- 10 J. Fleig, F. S. Baumann, V. Brichzin, H. R. Kim, J. Jamnik, G. Cristiani, H. U. Habermeier and J. Maier, *Fuel Cells*, 2006, **6**, 284–292.
- 11 F. S. Baumann, J. Fleig, M. Konuma, U. Starke, H. U. Habermeier and J. Maier, *J. Electrochem. Soc.*, 2005, **152**, A2074–A2079.
- 12 F. Baumann, J. Fleig, G. Cristiani, B. Stuhlhofer, H.-U. Habermeier and J. Maier, *J. Electrochem. Soc.*, 2007, **154**, B931–B941.
- 13 A. Wedig, R. Merkle, B. Stuhlhofer, H.-U. Habermeier, J. Maier and E. Heifets, *Phys. Chem. Chem. Phys.*, 2011, **13**, 16530–16533.
- 14 J. J. Kim, M. Kuhn, S. R. Bishop and H. L. Tuller, *Solid State Ionics*, 2013, **230**, 2–6.
- 15 W. C. Chueh, A. H. McDaniel, M. E. Grass, Y. Hao, N. Jabeen, Z. Liu, S. M. Haile, K. F. McCarty, H. Bluhm and F. El Gabaly, *Chem. Mater.*, 2012, **24**, 1876–1882.
- 16 S. C. DeCaluwe, M. E. Grass, C. Zhang, F. E. Gabaly, H. Bluhm, Z. Liu, G. S. Jackson, A. H. McDaniel, K. F. McCarty and R. L. Farrow, *J. Phys. Chem. C*, 2010, **114**, 19853–19861.
- 17 C. Zhang, Y. Yu, M. E. Grass, C. Dejoie, W. Ding, K. Gaskell, N. Jabeen, Y. P. Hong, A. Shavorskiy and H. Bluhm, *J. Am. Chem. Soc.*, 2013, **135**, 11572–11579.
- 18 A. Wedig, M. E. Lynch, R. Merkle, J. Maier and M. Liu, *ECS Trans.*, 2012, **45**, 213–224.
- 19 F. Ciucci, Y. Hao and D. G. Goodwin, *Phys. Chem. Chem. Phys.*, 2009, **11**, 11243–11257.
- 20 F. Ciucci, W. C. Chueh, D. G. Goodwin and S. M. Haile, *Phys. Chem. Chem. Phys.*, 2011, **13**, 2121–2135.
- 21 W. C. Jung and H. L. Tuller, *J. Electrochem. Soc.*, 2008, **155**, B1194–B1201.
- 22 W. C. Jung and H. L. Tuller, *Adv. Energy Mater.*, 2011, **1**, 1184–1191.
- 23 R. Merkle and J. Maier, *Phys. Chem. Chem. Phys.*, 2002, **4**, 4140–4148.
- 24 A. K. Opitz, M. P. Hörlein, T. M. Huber and J. Fleig, *J. Electrochem. Soc.*, 2012, **159**, B502–B513.
- 25 J. Jamnik and J. Maier, *Phys. Chem. Chem. Phys.*, 2001, **3**, 1668–1678.
- 26 M. Hendriks, J. Ten Elshof, H. Bouwmeester and H. Verweij, *Solid State Ionics*, 2002, **146**, 211–217.
- 27 A. K. Opitz and J. Fleig, *Solid State Ionics*, 2010, **181**, 684–693.
- 28 A. Rothschild, W. Menesklou, H. L. Tuller and E. Ivers-Tiffée, *Chem. Mater.*, 2006, **18**, 3651–3659.
- 29 S. Steinsvik, R. Bugges, J. Gjønnnes, J. Taftø and T. Norby, *J. Phys. Chem. Solids*, 1997, **58**, 969–976.
- 30 M. Burriel, G. Garcia, J. Santiso, J. A. Kilner, R. J. Chater and S. J. Skinner, *J. Mater. Chem.*, 2008, **18**, 416–422.
- 31 M. Gerstl, T. Frömling, A. Schintlmeister, H. Hutter and J. Fleig, *Solid State Ionics*, 2011, **184**, 23–26.
- 32 L. Wang, R. Merkle, J. Maier, T. Acartürk and U. Starke, *Appl. Phys. Lett.*, 2009, **94**, 071908.
- 33 L. Van der Pauw, *Philips Tech. Rev.*, 1958, **20**, 220–224.
- 34 J. Maier, *Physical chemistry of ionic materials: ions and electrons in solids*, Wiley, 2004.